Review

Jonas Kiemle, Philipp Zimmermann, Alexander W. Holleitner and Christoph Kastl*

Light-field and spin-orbit-driven currents in van der Waals materials

Abstract: This review aims to provide an overview over recent developments of light-driven currents with a focus on their application to layered van der Waals materials. In topological and spin-orbit dominated van der Waals materials helicity-driven and light-field-driven currents are relevant for nanophotonic applications from ultrafast detectors to on-chip current generators. The photon helicity allows addressing chiral and non-trivial surface states in topological systems, but also the valley degree of freedom in two-dimensional van der Waals materials. The underlying spin-orbit interactions break the spatiotemporal electrodynamic symmetries, such that directed currents can emerge after an ultrafast laser excitation. Equally, the light-field of few-cycle optical pulses can coherently drive the transport of charge carriers with sub-cycle precision by generating strong and directed electric fields on the atomic scale. Ultrafast light-driven currents may open up novel perspectives at the interface between photonics and ultrafast electronics.

Keywords: light-wave-driven currents; optoelectronics; photoemission; terahertz; topology; two-dimensional materials; ultrafast currents.

1 Introduction

In the past decade, layered van der Waals materials have regained significant interest because of their emergent optoelectronic properties when reduced to two-dimensional (2D) layers [1, 2]. The vast library of 2D materials comprises graphene, a zero-band-gap semiconductor [3], insulating wide-band-gap hexagonal boron nitride (hBN) [4], transition metal dichalcogenides (TMDs) – including insulators, semiconductors, semimetals, as well as true metals [5], and layered topological materials [6]. Due to their weak interlayer coupling, van der Waals materials can be combined (or stacked) into atomically sharp heterostructures and superlattices without the lattice matching constraints imposed by traditional thin film epitaxy [7]. This ability to create vertical heterostructures has been used, for example, in semiconducting TMDs to study photogenerated Coulomb-bound electron hole pairs, so-called interlayer excitons, featuring prolonged radiative lifetimes [8–10]. Furthermore, adjusting the twist angle between two adjacent layers opens up the possibility to engineer the lateral band structure towards collective electronic excitations and altered optical properties via the formation of in-plane moiré superlattices at will [11–13].

For optoelectronic applications, the tungsten- and molybdenum-based semiconductors, including MoS_2, $MoSe_2$, WS_2, and WSe_2, are particularly appealing [14]. In the monolayer limit, these prototypical TMDs are direct-gap semiconductors, whose optical properties are dominated by many-body exciton physics, even at room temperature [15, 16]. Due to their strong spin-orbit coupling, monolayer TMDs inherently intertwine angular momentum, out-of-plane spin, and crystal momentum degrees of freedom, such that under polarized optical excitation directed spin and charge currents can emerge [17–21]. Directly after a pulsed photoexcitation, the presence of a large density of (photogenerated) charge carriers can alter the Coulomb screening in monolayer TMDs [22–29], such that both the quasi-particle band gap and the excitonic binding energies are renormalized on femtosecond time scales. The renormalization effects are based upon an interplay of excitation-induced dephasing, phase-space filling and the screening of Coulomb interaction in combination with ultrafast non-radiative relaxation and recombination processes [22–26, 30]. Furthermore, monolayer TMDs exhibit valley-contrasting angular momentum

*Corresponding author: Christoph Kastl, Walter Schottky Institute and Physics Department, Technical University of Munich, Am Coulombwall 4a, Garching, 85748, Germany,
E-mail: christoph.kastl@wsi.tum.de. https://orcid.org/0000-0001-5309-618X
Jonas Kiemle and Philipp Zimmermann: Walter Schottky Institute and Physics Department, Technical University of Munich, Am Coulombwall 4a, Garching, 85748, Germany
Alexander W. Holleitner: Walter Schottky Institute and Physics Department, Technical University of Munich, Am Coulombwall 4a, Garching, 85748, Germany; Munich Center for Quantum Science and Technology (MCQST), Schellingstraße 4, München, 80799, Germany.

selection rules, allowing for valley-selective excitation with a corresponding out-of-plane spin orientation under circularly polarized excitation [31]. The optically induced excitonic valley polarization is relaxed within picoseconds due to exciton-mediated intervalley scattering [32]. Yet, the valley and spin polarizations of free carriers can persist up to nanoseconds [33–35], which in turn may drive valley and spin Hall currents [36]. Interestingly, upon resonant excitation with linearly polarized light, excitons can also be prepared in a coherent superposition state, which has however been shown to last only for a few hundred of femtoseconds [37]. In van der Waals heterostructures, transient absorption microscopy experiments revealed that the interlayer charge transfer takes place on a time scale of hundreds of femtoseconds up to one picosecond [38], prior to forming tightly bound interlayer excitons [39]. While the exciton lifetime in monolayer TMDs has been shown to range from a few picoseconds up to one nanosecond [40, 41], interlayer excitons in TMD heterostructures exhibit radiative lifetimes reaching one hundred nanoseconds due to a reduced spatial overlap of electron and hole wave functions [8]. Eventually, the photo-induced excess energy is transferred to the phonon bath as can be detected by bolometric currents [27, 42, 43].

Generally, there have been several reports on photocurrent and photoconductance phenomena in TMDs [14, 44–56]. The relevant timescales span from femtoseconds to nanoseconds (Figure 1) due to the complex excitonic relaxation cascade outlined above. The photovoltaic and lifetime-limited currents can be resolved up to a few picoseconds after an ultrafast photo-excitation of the TMDs. Photothermoelectric currents emerge on a timescale between hundreds of femtoseconds and several picoseconds after thermalization of the photoexcited charge carriers has taken place. The cooling of the photon bath can last from picoseconds to nanoseconds depending on the interfacial thermal conductance of the monolayer material to the substrate and to the metal contacts [57].

Correspondingly, the bolometric current can prevail up to several nanoseconds.

Apart from TMDs, topological insulators – narrow-gap semiconductors with conducting gapless states at their surface – also exhibit angular momentum selection rules due to an in-plane spin-momentum locking of the surface states [58–60]. The helical spin texture manifests itself in a surface transport that is sensitive to the helicity of the exciting light [61, 62]. Topological insulators, such as the layered van der Waals compounds Sb_2Te_3, Bi_2Te_3, Bi_2Se_3 or Bi_2Te_2Se, exhibit gapless surface states, which provide fast relaxation channels to the Fermi level. Therefore, in topological insulator thin films, the charge carrier dynamics after optical excitation are governed by a hot electron ensemble [63], in stark contrast to the excitonic response of TMDs. The spin and momentum depolarization have been shown to take place on a common sub-picosecond time scale as expected for spin-momentum locked surface states [60, 64, 65]. Correspondingly, time-resolved photocurrent measurements show that photogalvanic surface currents exhibit a quasi-instantaneous, sub-picosecond response time [62, 66, 67]. The hot electron ensemble prevails only on a picosecond timescale due rapid cooling via phonons and recombination via scattering between surface carriers and residual bulk carriers [63, 68–71], which gives rise to (ultrafast) photothermoelectric currents [62, 72]. For intrinsic and compensated topological insulators, where the Fermi level is adjusted into the gap and the bulk conductivity is suppressed [73, 74], extended lifetimes (nanoseconds to microseconds) have been reported for a surface photovoltage and associated photoconductivity due to spatial separation of photoinduced charges between the surface and the bulk [75–79].

Recent reports on graphene suggest that even attosecond dynamics can be explored in two-dimensional van der Waals materials with carrier-envelope phase stabilized lasers in the strong-field regime [80, 81]. This strong-field regime is achieved for decent peak electric fields of
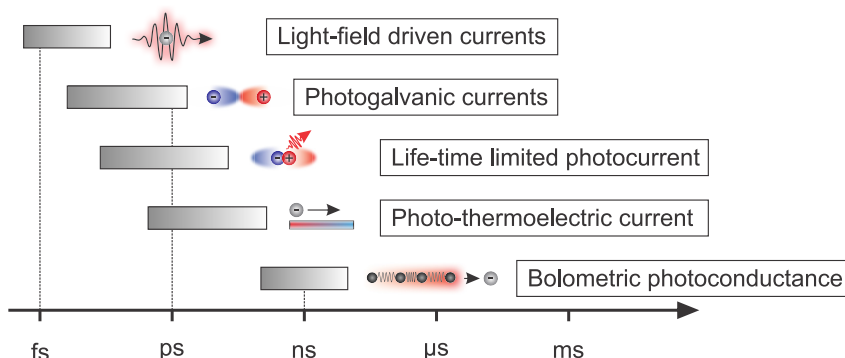

Figure 1: Time scales of ultrafast light-driven currents in low-dimensional van der Waals materials.

about 2 Vnm⁻¹ for a near-infrared few-cycle laser [81], which suggests the occurrence of light-field-driven currents, as reported mainly for bulk solids so far [82, 83–85], also in TMDs and further atomistic van der Waals materials. Nowadays, electron dynamics which are directly driven via the amplitude and phase of optical fields represent the fastest experimentally accessible time scale (Figure 1). The study of light-driven currents is of fundamental interest for the understanding of the underlying quantum dynamics and for the development of future ultrafast optoelectronics beyond the current state of the art.

This review gives an overview on spin-orbit-driven and ultrafast topological currents in van der Waals materials. We first present briefly general symmetry considerations for light-driven currents in solid-state materials, where photocurrents are formally described as a nonlinear response driven by the optical field (Section 2). For an extensive discussion of such high-frequency nonlinear transport, we refer to the review by Glazov and Ganichev [86]. In this context, we discuss the phenomenology of the photogalvanic effect and of coherently controlled currents, which are second- and third-order phenomena, respectively. Of particular relevance for (opto)spintronic applications are helicity-driven currents in spin-orbit coupled systems [14, 15, 87], where the coupling between the angular momenta of photons and electrons controls spin and charge currents. Therefore, we present selected examples for helicity-driven currents in van der Waals materials in Section 3, including TMDs with their coupling of valley and out-of-plane spin, topological insulators with their in-plane spin-momentum locking, and Weyl semimetals with their chiral electron states. In particular, we discuss how anomalous Hall photocurrents can arise from Berry curvature effects in TMDs and Weyl semimetals. In the last section of the review, we illustrate how strong and ultrafast light-fields are employed to directly drive currents at optical frequencies (Section 4), and how such light-field-driven currents could be integrated into terahertz (THz) circuits for next generation high-speed optoelectronics (Section 5).

2 General symmetry considerations for light-driven currents

On a very general basis, light-driven currents can be treated as a nonlinear response of the electron system to the optical field [86]. By expanding the time and spatially dependent electric current density $\boldsymbol{j}(\boldsymbol{r}, t)$ in a power series of the external alternating electric field $\boldsymbol{E}(\boldsymbol{r}, t) = \boldsymbol{E}(\omega, \boldsymbol{q})e^{-i\omega t + i\boldsymbol{q}\boldsymbol{r}} + \boldsymbol{E}^*(\omega, \boldsymbol{q})e^{+i\omega t - i\boldsymbol{q}\boldsymbol{r}}$, one can identify the different nonlinear contributions to the electronic response. Based on symmetry principles and without prior knowledge about the microscopic details, general statements can be made how the direction and magnitude of the photo-induced current depend on the underlying crystal symmetry, the angle of incidence, the photon momentum, and the polarization of the incident light. Table 1 summarizes the most common second and third order effects, which can result in both AC and DC electronic responses.

In the following, we focus on the DC response, which can be detected as the photocurrent in an optoelectronic experiment. The leading order DC response to an oscillating electric field is the so-called photogalvanic effect, which can be formally written as [59, 88, 89]

$$j_\alpha = \sigma_{\alpha\beta\gamma}(\omega)E_\beta(\omega)E_\gamma^*(\omega). \tag{1}$$

The Greek subscripts denote Cartesian coordinates. The term $\sigma_{\alpha\beta\gamma}(\omega)$ describes the third-rank photogalvanic tensor. The electric field components $E_\beta(\omega)$ are described by plane waves with $\boldsymbol{E}(t) = \boldsymbol{E}(\omega)e^{i\omega t} + \boldsymbol{E}(\omega)^*e^{-i\omega t}$. While the current switches sign under inversion, the second order product of the electric field components does not, such that the photogalvanic effect can only arise in non-centrosymmetric materials, in other word only for broken inversion symmetry [88]. Microscopically, it can originate from an asymmetric excitation in k – space due to optical selection rules, an asymmetric excitation via intermediate states, or from asymmetric scattering after the optical excitation [89–

Table 1: Summary of second and third-order light-driven currents.

	Second order	Third order
AC response	Second harmonic generation, Optical rectification	Third harmonic generation, Two photon absorption, Frequency mixing Optically induced Faraday/Kerr effect
DC response	*Photogalvanic effect, Photon drag effect*	*Coherent control, (Hall) photoconductivity*

91]. By requiring the current to be real, the response can be rewritten as [88, 89]

$$j_\alpha = \gamma_{\alpha\beta} i (\boldsymbol{E} \times \boldsymbol{E}^*)_\beta + \chi_{\alpha\beta\gamma}\left(E_\beta E_\gamma^* + E_\gamma E_\beta^*\right), \qquad (2)$$

with the frequency dependence omitted for brevity. The components $\gamma_{\beta\gamma}$ and $\chi_{\alpha\beta\gamma}$ form a second-rank pseudo-tensor and third-rank tensor, respectively. The first term describes the helicity-dependent circular photogalvanic effect, and it switches sign between circular left- and right-handed polarization [86, 88]. Microscopically, the absorption of circularly polarized light results in a transfer of angular momentum from photons to electrons [31]. At the presence of spin-orbit coupling, directed currents can emerge under a circularly polarized excitation due to the optical spin orientation via interband transitions [92]. Furthermore, free-carrier intraband absorption of circularly polarized radiation can generate a directed current purely based on an orbital mechanism without the presence of spin-orbit coupling [91]. The second term in Eq. (2) is helicity-independent, and it describes the linear photogalvanic effect [86, 88].

Photogalvanic effects have been studied extensively for 2D electron gases in III-V semiconductors [89]. Furthermore, they have been applied both experimentally and theoretically to van der Waals materials, including 3D topological insulators [58, 59, 62, 93–99], 2D TMDs [17, 18, 100], WS_2 nanotubes [101], polar van der Waals materials [102, 103], and layered Weyl semimetals [104–107]. Photogalvanic currents form an effective toolbox to explore fundamental optoelectronic symmetries. For example, single-layer graphene is inversion symmetric, and a circular photogalvanic effect becomes possible only for a reduced symmetry, which is achieved at crystal edges or by a substrate-induced symmetry breaking [108, 109]. A further example is the topological insulator Bi_2Se_3, where the bulk inversion symmetry precludes the occurrence of a bulk photogalvanic effect by symmetry [94]. At the surface, however, the crystal symmetry is reduced, and a photogalvanic effect becomes symmetry-allowed under an oblique angle of incidence [61]. Therefore, the photogalvanic effect can selectively probe surface related phenomena in such typical topological insulator compounds [95, 96, 110]. Moreover, photogalvanic effects can provide a direct measure of the Berry curvature in materials with non-trivial band topology [111, 112].

General care must be taken to differentiate photogalvanic currents from photon drag currents. For the latter, the transfer of momentum from photons to electron drives the electric current. The photon drag effect shows a qualitatively similar polarization dependence as the photogalvanic effect, but a distinctly different dependence on photon momentum $\boldsymbol{q}$ [86, 113–115].

$$j_\alpha = \phi_{\alpha\beta\gamma\mu}(\omega) q_\mu E_\beta(\omega) E_\gamma^*(\omega). \qquad (3)$$

Therefore, photon drag currents are symmetry allowed also in centrosymmetric crystals, because both the photon momentum and the electric current switch sign under a spatial inversion.

The third order effects are related to the class of four-wave-mixing effects, where three fields interact and give rise to the fourth one [86]. In contrast to the photogalvanic effect, which is second order in the electric field, the third order effects are generally symmetry allowed in both centrosymmetric and non-centrosymmetric systems [86]. Of particular relevance is the so-called coherent control of ballistic currents [115]. Most commonly, a one- and two-photon absorption at frequencies ω and 2ω was studied both theoretically and experimentally [116–120]. Microscopically, the coherently controlled current injection is a consequence of quantum interference between the one- and two-photon interband transition (Figure 2A) [121]. The one- and two-photon processes connect the initial state to final states which are degenerate in energy but of different parity [116, 121]. Then, the interference between the one- and two-photon absorption processes can lead to localized electronic excitations in momentum space. For example, theoretical calculations for monolayer WSe_2 predict that a polar distribution of carriers can be excited coherently at each valley in the Brillouin zone (Figure 2B) [122]. In simple words, for such a polar distribution, the group velocity of the excited carrier ensemble does not average out across the Fermi surface and a net charge current arises. The carrier distribution in momentum space and the corresponding injected current can be manipulated via the polarization, the intensity, and the relative phase difference $\Delta\phi = 2\phi_\omega - \phi_{2\omega}$ of the pump fields ω and 2ω. The charge current injection rate due to a two-color photoexcitation $\boldsymbol{E}(t) = \boldsymbol{E}(\omega)e^{i\omega t} + \boldsymbol{E}(2\omega)e^{2i\omega t} + c.c.$ is described as [116]

$$\frac{dj_\alpha}{dt} = \eta_{\alpha\beta\gamma\delta}(\omega) E_\beta^*(\omega) E_\gamma^*(\omega) E_\delta(2\omega) + \text{c.c.}, \qquad (4)$$

where c.c. denotes the complex conjugation. The forth rank tensor $\eta_{\alpha\beta\gamma\delta}(\omega)$ describes coherent one- and two-photon injection and includes contributions from both electrons and holes [116].

Such coherently controlled charge currents have initially been predicted and observed for bulk semiconductors, such as GaAs or Si [116, 118, 119, 121, 123], and later also for one-dimensional and two-dimensional nanoscale materials, such as carbon nanotubes, semiconductor
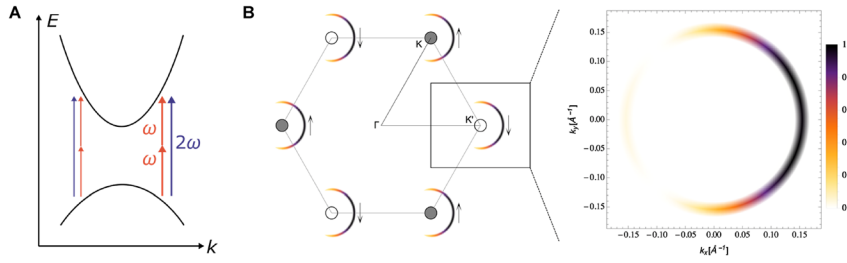
Figure 2: Coherent control of injection currents. (A) Schematic depiction of a coherent one-photon (2ω) and two-photon (ω) absorption process in a two-band model. The coherent superposition leads to an asymmetric final state amplitude in k-space, as indicated by the width of the arrows. (B) Calculated carrier distribution near the K and K' valleys of WSe$_2$ for a coherent one- and two-photon absorption process with 50 fs optical pulses. The color scale denotes the carrier population after the pulsed excitation. The finite width of the carrier distribution is due the finite bandwidth of the laser pulse. For each valley, the carriers are excited with the same polar distribution (right panel). Then, the group velocities around each valley do not average out, and a net current is injected. For the model calculation, the phase difference between the one- and two-photon fields is assumed to be $3\pi/2$, and the one-photon excitation energy is 1.8 eV. Reproduced with permission [122]. Copyright 2019, American Physical Society.

nanowires or graphene [115, 117, 120, 124–126]. Similarly, coherent injection of spin and valley currents has been proposed for two-dimensional van der Waals materials [122, 127, 128]. Experimentally, the coherent control was detected either statically by measuring the net DC-current between a source and drain electrode [123, 126] or dynamically by detecting the emitted THz field due to the injected current pulses in the material [129]. By contrast, time-resolved angle-resolved photoemission spectroscopy (tr-ARPES) can directly image the non-equilibrium carrier distribution in k-space on femtosecond timescales [43, 85, 130–133]. Combining coherent control to controllably inject carriers in momentum space with time- and momentum-resolved spectroscopy allows to observe the relaxation dynamics in real-time and paves the way to precisely study fundamental electron-electron as well electron-phonon interactions in low-dimensional van der Waals materials [131].

Lastly, we consider the case of photoconductivity, which can be described within the above framework as a third order nonlinearity. In that case, one of the fields is static $\boldsymbol{E}(\omega = 0, \boldsymbol{q} = 0)$, while the remaining two fields alternate at the same frequency with $\boldsymbol{E}(\omega, \boldsymbol{q})$. The resulting DC response is described by

$$j_\alpha = \sigma_{\alpha\beta\gamma\delta}(\omega)E_\beta(\omega, \boldsymbol{q})E_\gamma^*(\omega, \boldsymbol{q})E_\delta(\omega = 0, \boldsymbol{q} = 0). \quad (5)$$

In close analogy to the photogalvanic effect, the photoconductivity can be separated into symmetric and antisymmetric contributions under permutation of β and γ, giving rise to linear and circular photoconductivities, respectively [86]. A circular photoconductivity, also termed photovoltaic Hall effect, has been predicted for example in graphene [134], and it results in a current flow perpendicular to the static electric field under normal incidence of the radiation

$$\boldsymbol{j} \propto \boldsymbol{E}(\omega = 0, \boldsymbol{q} = 0) \times (\boldsymbol{E}(\omega, \boldsymbol{q}) \times \boldsymbol{E}^*(\omega, \boldsymbol{q})). \quad (6)$$

The corresponding DC (Hall) photoconductivity emerges despite the absence of a uniform external magnetic field. Importantly, the direction of the Hall current reverses sign, if the helicity of the optical excitation is reversed. Microscopically, the photoconductivity can arise, for example, due to the coherent dressing of the electronic structure via Floquet states [134] or due to a combination of an optical spin orientation and a spin Hall effect [20]. Lastly, we note that the above formalism applies strictly only to homogeneous media under a homogeneous excitation [88]. For nanoscale materials and devices, local anisotropies, such as edges, metal contacts, built-in potentials, or density gradients from a focused excitation, can give rise to a modified photoresponse due to local ballistic, drift, and diffusion currents [14, 47, 135–140].

3 Photon helicity-driven currents

In the following, we focus on selected examples of helicity-driven currents in van der Waals materials. Having established the phenomenological description of light-driven currents, we discuss the underlying microscopic mechanisms as well as experimental schemes to detect (ultrafast) photocurrents and photoconductivities in van der Waals materials. For TMDs, the spin-orbit coupling results in a direct locking of out-of-plane spin and valley degrees of freedom. Then, under a circularly polarized excitation pure out-of-plane spin and valley currents emerge (Section 3.1). For topological insulators, we discuss ultrafast coupled charge and spin currents. These ultrafast currents stem from the helical surface states, where in-plane spin and momentum are locked perpendicularly and consequently their relaxation is governed by a common decay time (Section 3.2). In topological semimetals, the coupling between photon and electron

chirality results in helicity-driven Hall currents, which arise from the underlying Berry curvature monopoles of the Weyl points (Section 3.3). Controlling the flow of charge, spin, and momentum in van der Waals materials by optical means can be utilized in (opto-) spintronic devices to inject, manipulate, or detect spin, charge, and orbital currents [14, 15, 137, 141].

3.1 Valley optoelectronics in TMDs

The prototypical TMD semiconductors, such as MoS_2, WS_2, $MoSe_2$ and WSe_2, exhibit a hexagonal crystal structure (Figure 3A). The optoelectronics of monolayer TMDs are dominated by the inequivalent K and K' valleys located at the edges of the hexagonal Brillouin zone (Figure 3B). Furthermore, due to the inherently broken inversion symmetry in monolayer TMDs, the band edges of the K and K' valleys exhibit a nonzero Berry curvature $\Omega_n(\mathbf{k})$. The Berry curvature impacts the electronic transport via a quantum correction to the band velocity [142–144]. For an electron with wavevector $\mathbf{k}$ and band index n, the band velocity reads

$$v_n(\mathbf{k}) = \frac{\partial E_n(\mathbf{k})}{\hbar\,\partial\,\mathbf{k}} - \frac{e}{\hbar}E \times \Omega_n(\mathbf{k}). \tag{7}$$

In a simple view, the Berry curvature acts as a pseudo-magnetic field in momentum space. It results in an anomalous velocity which is always transverse to an externally applied electric field E. As a consequence of time-reversal symmetry, the Berry curvature is exactly opposite in the two valleys with $\Omega(K) = -\Omega(K')$, and charge carriers from K and K' valleys acquire an opposite

anomalous velocity, resulting in the so-called valley Hall effect (Figure 3C) [145]. The finite and opposite Berry curvature of the K and K' valleys provides a versatile route to electrically generate charge-neutral valley currents via the valley Hall effect and allows to detect valley currents, for example, via the corresponding inverse valley Hall effect [146, 147]. Under time-reversal symmetric conditions, the total transversal charge current and therefore the Hall voltage is zero, since the charge carriers from opposite valleys are driven towards opposite edges of the conducting channel. However, due to the locking of spin and valley in monolayer TMDs, this charge neutral Hall current results in the accumulation of an opposite spin polarization at opposite edges (Figure 3C), which is also called a spin Hall effect. Such a spin-valley accumulation has been confirmed by magneto-optical Kerr microscopy both for electrons and holes in gate-tuned monolayer WSe_2 [19]. The spin Hall effects is not unique to strictly spin-valley coupled systems, but it is a general consequence of spin-orbit interaction [148]. Importantly, the intrinsic Berry curvature contributions to the spin Hall conductivity need to be carefully distinguished from extrinsic contributions, such as side jump and skew scattering. The latter arise for example by spin- or valley-dependent scattering of charge carriers at atomistic defects, and they depend on details of defect density and defect potential shape [143, 149–151]. In solids with broken time reversal symmetry, typically a ferromagnetic phase, these processes result in the anomalous Hall effect [152], since – in a simple picture – contributions from spin-up and spin-down electrons do not average out. For non-magnetic materials, time-reversal symmetry of the electron ensemble in the crystal can effectively be broken by an optically injected non-
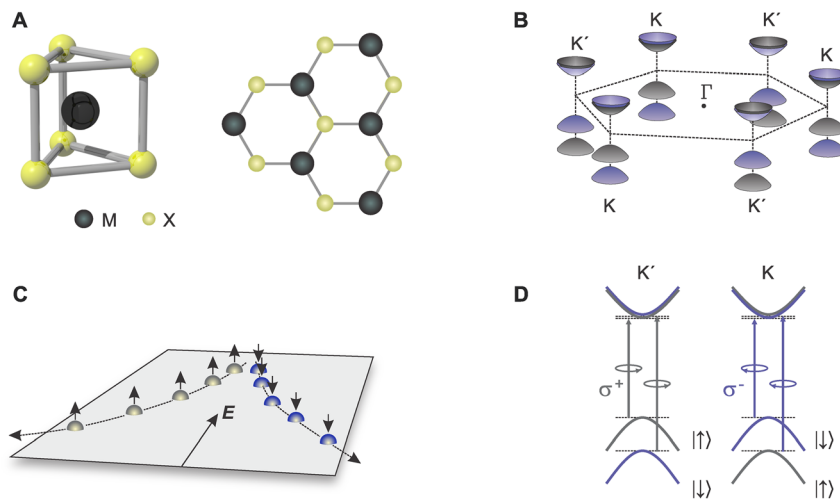

Figure 3: Valley optoelectronics in monolayer TMDs. (A) Hexagonal crystal structure of monolayer TMDs. Black (yellow) denotes the metal (chalcogen) atoms. (B) In the hexagonal Brillouin zone, the K and K' valleys are inequivalent due to the broken inversion symmetry of the monolayer. This results in an opposite Berry curvature of the bands in opposite valleys. (C) Schematic of the valley Hall effect. Under an applied external field, the valley-contrasting Berry curvature drives opposite Hall currents. Under equilibrium conditions, the overall current is charge neutral, but a pure spin-valley current arises. (D) A circularly polarized excitation couples selectively to K or K' valley due to angular momentum selection rules. Then, a net charge current can arise due to the valley Hall effect.

equilibrium spin and charge distribution in the Brillouin zone, leading to a Hall photoconductivity as in Eq. (6). For TMDs, the valley population can be modified optically by circular polarized excitation, as a consequence of valley-selective angular momentum selection rules (Figure 3D) [31]. These optical selection rules are exact for a resonant excitation [145], and a substantial valley polarization can be achieved for time scales shorter than the valley polarization time [145, 153]. Under a linearly polarized excitation, electrons and holes are excited equally in both valleys and the Hall voltage vanishes. By contrast, under a circularly polarized optical excitation, the optically induced valley polarization breaks time-reversal symmetry. At the presence of an external longitudinal bias, electrons (or holes) from the optically pumped valley acquire a transversal velocity and accumulate at one edge. Then, a non-zero Hall voltage can be detected. Using an optoelectronic read-out scheme, Mak et al. demonstrated a helicity-driven Hall voltage for n-type monolayer MoS_2 [20]. The observation of the net Hall voltage has been interpreted to be a consequence of the optically induced valley polarization of free charge carriers in combination with the intrinsic valley Hall effect [20]. It is worth noting that recent theoretical studies suggest a partial cancelation of the Berry curvature and the side jump contribution for a photon drag induced valley Hall effect of massive 2D Dirac electrons, such that the skew scattering should dominate [151].

For low doping and small excitation densities below the Mott transition [154], the optoelectronic properties of TMDs are expected to be dominated by tightly bound neutral excitons with binding energies as large as 0.3 –1 eV [16, 155]. In this context, polarization-resolved photoluminescence mapping of monolayer MoS_2 channels revealed a valley-selective diffusion of excitons on a micrometer scale, which was attributed to an exciton Hall effect [147, 156]. For the neutral excitons, an anomalous transversal velocity cannot result from an external electric field, but rather from the temperature or density gradient of excitons [156]. For exciton-polaritons strongly coupled to a microcavity photon mode, an optical valley Hall effect was observed in monolayer $MoSe_2$, enabled by the long-range propagation of exciton-polaritons excited at a finite wave vector [157].

In even-numbered TMD layers, e. g., bilayer MoS_2, inversion symmetry of the crystal is restored, and consequently $\Omega(K) = \Omega(K')$ such that the Berry curvature-induced valley current vanishes [158]. However, external stimuli, such as electric displacement fields, strain or substrate interactions, can be used to break inversion symmetry on demand [158, 159]. In this context, a gate-voltage-dependent spin accumulation was observed at the edges of a MoS_2 bilayer field effect transistor device as evidenced by the magneto-optical Kerr effect [159]. In multilayer bulk samples the inversion symmetry is gradually restored [160], and furthermore the indirect band does not involve K and K' valleys, which results overall in a very small or even zero Berry curvature.

Recent theoretical studies suggest an even richer picture of Hall currents in two-dimensional TMDs [36, 158, 161]. For monolayer MoS_2 supported on a substrate, the broken mirror symmetry perpendicular to the layers allows spin-orbit coupling terms that substantially modify the Berry curvature, in particular for the conduction band where the intrinsic spin-orbit coupling is small [161]. Similarly, a further theoretical study predicted Berry curvature terms that originate from inversion-asymmetric spin-orbit interactions in gated structures [36]. This additional Berry curvature manifests in a spin-orbit coupling-induced valley Hall effect, which can be dominant in gated or polar TMDs [36]. For bilayer MoS_2, the effect of interlayer couplings was studied by considering $2H$ and $3R$ bilayers, and a large tuneability of the valley Hall effect was predicted for double gated $2H$-MoS_2 bilayers [158].

Ultimately, generating light-driven, pure valley currents of free carriers requires the dissociation of the excitons [53]. In WS_2-WSe_2 heterostructures the type-II band alignment favors interlayer charge transfer of optically excited electrons into the WS_2 layer. Here, a spin-valley diffusion of optically excited free holes has been observed in the WSe_2 layer with a valley diffusion length on the order of 20 μm and an apparent valley life time exceeding 10 μs [162]. Furthermore, a valley-dependent contribution to the longitudinal photocurrent is observed in monolayer MoS_2 with an applied external magnetic field. The observed helicity-dependent current is attributed to an unbalanced transport of valley-polarized trions due to the opposite Zeeman shifts of the K and K' valleys, and it may provide an alternative route to electronically read-out optically imprinted valley information [21].

3.2 Ultrafast helicity control of surface currents in topological insulators

Layered three-dimensional topological insulators, such as Bi_2Te_3, Bi_2Se_3, and Bi_2Te_2Se have emerged as promising materials for optoelectronic applications from infrared down to THz frequencies [66, 87, 94]. As a consequence of strong spin-orbit coupling, these materials exhibit

topological surface states forming a Dirac cone with helical spin texture, which interconnect the band gap between valence and conduction bands of the bulk band structure [163, 164]. Charge carriers at the surface states are endowed with in-plane spin-momentum locking, providing a platform for ultrafast optical control of spin and charge currents in topological insulators. In a simple picture, circularly polarized light can induce a net spin polarization after excitation via angular momentum selection rules [64]. Then, the in-plane spin-momentum locking drives a surface photocurrent, which is sensitive to the helicity of the exciting light [58, 59, 61, 62]. Notably, for a dominating photogalvanic effect, bulk contributions to the photocurrent are absent in inversion symmetric compounds, such as tetradymite chalcogenides (cf. Section 2) [89]. At the material surface, however, the crystal symmetry is reduced and a net photogalvanic current becomes symmetry-allowed for obliquely incident excitation [58, 59, 61].

In the following, we discuss exemplarily an on-chip pump-probe photocurrent spectroscopy, which allows to resolve the femtosecond temporal dynamics of photocurrents in topological insulators directly at room temperature. Briefly, a thin Bi_2Se_3-film is placed between two coplanar striplines, acting as high-frequency transmission lines (Figure 4A and 4B). Upon excitation with a circularly polarized femtosecond pump laser pulse (E_{photon} = 1.5 eV) at oblique angle of incidence, the in-plane response across the Bi_2Se_3-film couples into the striplines. Consequently, an electromagnetic transient proportional to the initial current propagates along the striplines. After a time delay Δt, an additional femtosecond probe laser pulse triggers an ion-implanted silicon Auston switch for the read-out of the electric field within the transient. Thus, the time-resolved, light-induced current response $I_{sampling}(\Delta t)$ can be monitored for different helicities (right- versus left-circular polarization) of the exciting light, revealing the helical symmetry of the surface states. In particular, the time-averaged photocurrent versus photon polarization follows a sinusoidal behavior (Figure 4C). For typical experimental conditions, where the excitation polarization is adjusted via a quarter waveplate, the photocurrent is modeled as

$$I_{photo} = C\sin(2\alpha) + L_1\sin(4\alpha) + L_2\cos(4\alpha) + D. \quad (8)$$

Here, α is the angle of the quarter waveplate, altering the polarization state of the light, C is the amplitude of the helicity dependent current, L_1 and L_2 are the amplitudes of the photocurrents that depend on linear polarization, and D is the polarization-independent current [58, 61, 62]. Peculiarly, the time-resolved photocurrent measurements show that the laser-induced currents exhibit a quasi-instantaneous response on a time scale of about 1 ps, with a photocurrent sign and amplitude following the polarization of the incident light (Figure 4D and 4E). For later times ($\Delta t \geq 5$ ps), the helicity-induced spin information is lost by
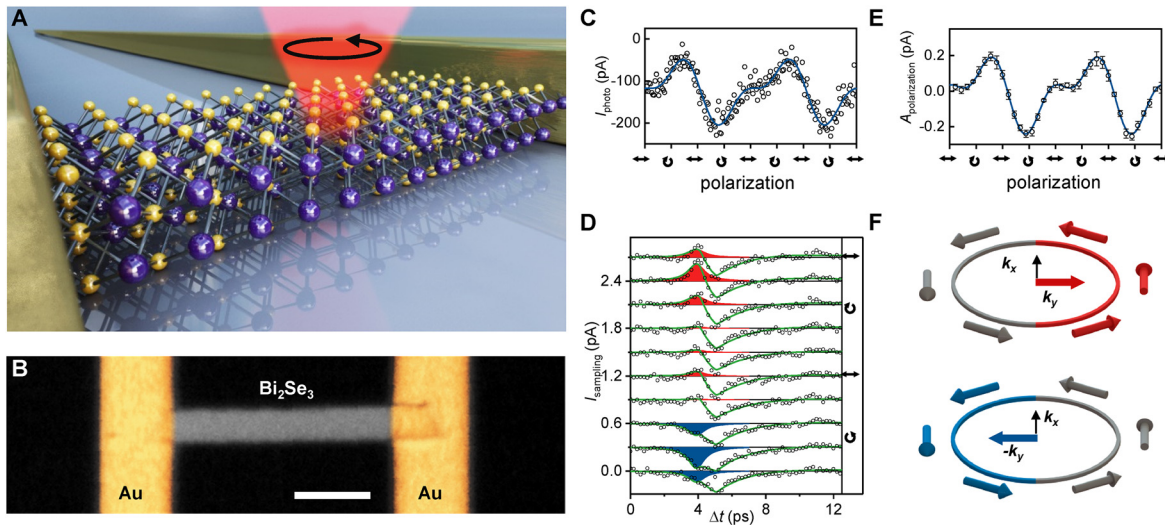

Figure 4: Helicity-control of ultrafast currents in topological insulators. (A) Helical excitation controls surface currents in topological insulators. (B) Optical microscope image of a Bi_2Se_3 thin-film embedded into a THz-stripline circuit. Scale bar, 5 μm. (C) Time-averaged photocurrent I_{photo} versus photon polarization. (D) Time-resolved photocurrent $I_{sampling}$ at the center of the Bi_2Se_3-film for varying laser polarization. Solid lines are fits to the data, blue and red areas display the polarization-controlled ultrafast currents. Data are equidistantly displaced for clarity. (E) Fitted amplitude of $I_{sampling}$ for a time delay of Δt = 4 ps versus photon polarization. (F) Schematic of the photogalvanic current in the direction of k_y to the right contact (red) or $-k_y$ to the left contact (blue) with an in-plane spin polarization. Reproduced and adapted under the terms of the Creative Commons CC BY 4.0 license [62]. Copyright 2015, Nature Publishing Group.

spin depolarization and intraband cooling, resulting in an onset of polarization-independent surface and bulk currents with a lifetime of several picoseconds, consistent with results from tr-ARPES [63, 69, 71]. A closer look at the fast polarization-dependent response, considering the dispersion and attenuation of the wave-guides, revealed an upper bound of 670 fs [66]. This short time scale suggests that the helicity-dependent photocurrents are limited by spin and momentum depolarization (Figure 4F) [62, 64]. At the used excitation energy of 1.5 eV, optical transition between surface as well as bulk states are possible, which can all contribute to the photocurrent generation via photogalvanic or photon drag effects. Several studies identified a photogalvanic effect due to asymmetric optical transitions between the topological surface states and bulk bands via their characteristic Fermi level and wavelength dependence [93, 97, 165, 166]. By contrast, another study inferred from far field THz emission spectroscopy a dominating circular photon drag effect, but the individual contributions from surface and bulk states could not be resolved [98].

Light-driven currents in topological insulators were also studied indirectly by electrooptic sampling of the emitted THz radiation after optical pumping, which revealed femtosecond surface shift currents and ultrafast transient THz photoconductivity [67, 167, 168]. Furthermore, tr-ARPES experiments demonstrated that interband

transitions at mid-infrared energies below the bulk gap generate polar carrier distributions of surface states in k-space on a picosecond timescale, suggesting concurrent photogalvanic surface currents [65, 70]. Very recently, ARPES studies demonstrated that the k-space distribution of surface states can even be manipulated coherently at a THz interband excitation in the strong-field limit (cf. Section 4) [85]. Overall, the picosecond response time of the helical surface currents proves the foreseen potential of topological insulators to be promising materials for high-speed optoelectronic applications from infrared down to THz frequencies [78, 87, 94, 169].

3.3 Helicity-driven Hall currents in Weyl semimetals

Weyl semimetals, a novel class of quantum materials exhibiting topological protection, are proposed to have an electronic structure beyond that of prototypical topological insulators. Their electronic structure features three-dimensional linear band crossings between valence and conduction bands creating bulk Weyl nodes associated with a topological charge [170, 171]. The Berry curvature $\Omega_n(k)$ of the bands diverges near the topological Weyl points giving rise to a plethora of predicted optoelectronic phenomena, including quantized photogalvanic effects,
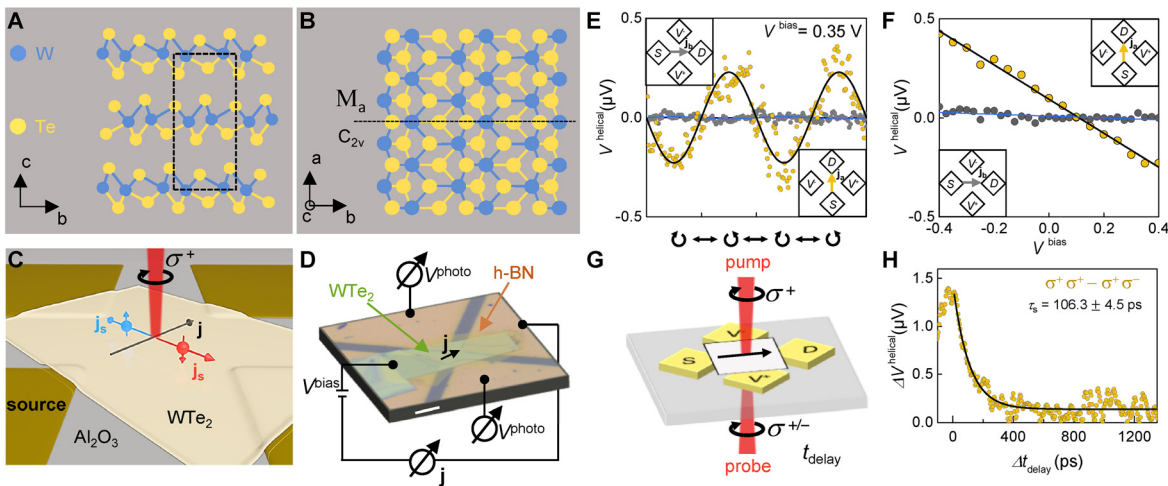

Figure 5: Photo-induced Hall effect in few-layer WTe$_2$ at room temperature. (A) Side view on the crystal structure of bulk T_d – phase WTe$_2$. Here, a and b denote the in-plane and c the out-of-plane crystal axis directions. In the T_d – phase, inversion symmetry is broken along the b axis. (B) Top view of the crystal structure of T$_d$ – WTe$_2$. The crystal exhibits a mirror plane M$_a$ orthogonal to the a-axis. (C) and (D) Schematic of an anomalous Hall effect in a four-terminal circuit induced by illumination with circularly polarized light. A longitudinal bias current is applied and the transversal photo-induced Hall voltage is measured. The a and b crystal axes of the WTe$_2$ are aligned along the contacts. (E) and (F) Anisotropic photo-induced Hall voltage as function of circular polarization and bias voltage. For a current applied along the b-axis, no Hall effect is observed, and the photo-induced Hall effect is linear in bias voltage. (G) and (H) Optoelectronic pump-probe scheme to read out the ultrafast dynamics of the photo-induced Hall effect. Reproduced with permission [181]. Copyright 2019, American Physical Society.

anomalous Hall effects [104, 172], and selective coupling between photon and Weyl Fermion chirality [112, 173]. For the point groups containing improper symmetry operations, in particular combinations of mirror and rotation symmetries, it has been shown theoretically that corrections to the minimal Weyl model, namely a tilt of the Weyl cone as well as second and third order terms, prevent cancellation of the photocurrent contributions from the Weyl cones of opposite chirality [106, 107, 174]. Along this line, so called type-II Weyl semimetals exhibit Weyl cones in the bulk that are tilted over one side, and within the class of TMDs $MoTe_2$ and WTe_2 were identified as potential candidates [175]. WTe_2 stands out from the family of layered TMDs by means of a structural anisotropy as it crystallizes in an orthorhombic T_d-phase, which is stable at room temperature (Figure 5A). The lattice of WTe_2 consists of tree atomic layers (W – Te – W) forming a distorted hexagonal lattice where the W atoms dimerize into a chain along the crystallographic a-axis. As a result, inversion symmetry in WTe_2 is intrinsically broken along the b-axis (Figure 5B), suggesting a non-trivial spin-resolved dipolar Berry curvature $\Omega_n(k)$ within the Brillouin zone [111, 176]. Due to the Berry curvature dipole, a nonlinear, anomalous Hall effect arises in WTe_2, although time-reversal symmetry still dictates overall a zero integrated Berry curvature [177, 178]. Recent theoretical work suggests that extrinsic contributions to the Hall conductivity enter the nonlinear Hall effect even in the leading order, such that disorder induced skew scattering and side jumps may become comparable to the intrinsic Berry curvature contributions [179]. Therefore, as in the case of the linear anomalous Hall effect with broken time-reversal symmetry [152, 180], it will be necessary to carefully distinguish between such extrinsic and intrinsic contributions.

In close analogy to the valley Hall effect discussed above, a circularly polarized optical excitation can effectively break time-reversal symmetry due to the Berry curvature-dependent chiral selection rules of the Weyl points (Figure 5C). For monolayer WTe_2, it was shown that the Berry curvature dipole can be electrically tuned by a displacement field leading to a circular photogalvanic effect when inversion symmetry is broken by an out-of-plane electric field [111]. By contrast, the intrinsically broken inversion symmetry of few-layer WTe_2 is a promising platform for lightwave and Berry phase-driven spin- and current-transport phenomena, e. g., giving rise to a photon-helicity-induced linear Hall effect at room temperature [181].

Experimentally, the optoelectronic transverse conductivity in few-layer WTe_2 can be accessed using a four-terminal contact geometry (Figure 5D). In a first step, the semimetal is aligned onto pre-defined Ti/Au electrodes and

covered by a thin sheet of hBN using mechanical exfoliation. The orientation of the crystallographic axis a is chosen to match the axis of two opposing electric contacts, which is verified by polarization-resolved Raman spectroscopy [181, 182]. A laser ($E_{photon} = 1.5\,eV$) is focused at the center of the WTe_2-film and an external (longitudinal) bias V_{bias} is applied between source and drain along the crystal a-axis, while the photo-induced (transversal) voltage V_{photo} is measured for different polarizations of the incident light. Peculiarly, the transversal voltage V_{photo} changes sign with changing laser helicity (right- versus left-circular polarization) and depends linearly on the applied longitudinal bias V_{bias} (Figure 5E and 5F). Importantly, as the bias is applied perpendicular to the WTe_2 a-axis, no distinct helicity-dependent transverse photovoltage occurs, which is consistent with a non-trivial dipolar Berry curvature at the Fermi surface of WTe_2 [176]. To determine the characteristic timescales of longitudinal bias current and photo-induced voltage, a time-resolved optoelectronic autocorrelation of the spin and charge dynamics can be employed (Figure 5G). While the transverse helicity-induced photovoltage V_{photo} decays exponentially on a timescale of $\tau_{slow} \sim 100\,ps$ (Figure 5H), the decay time of the photo-induced bias current is determined to be as fast as $\tau_{fast} \sim 2\,ps$. The fast response τ_{fast} of the longitudinal current can be interpreted as an instantaneous increase of photoconductance, limited by the phonon-mediated charge carrier relaxation to the Fermi energy [183, 184]. In contrast, the long timescale τ_{slow} is likely to stem from the excited nonequilibrium spin density on the Fermi surface after the initial charge carrier thermalization, which subsequently is driven by an anomalous velocity proportional to the anisotropic Berry curvature [142, 181]. Thus, time-integrated, as well as time-resolved photocurrent spectroscopy facilitate the observation of phenomena related to quantum geometrical phases in Weyl semimetals and topological materials up to room temperature.

4 Light-field-driven currents

The advent of ultrafast and strong light fields that span from the THz – to the UV-regime has ushered in a new era of coherent light-matter interaction as well as light-matter manipulation [185, 186]. For example, attosecond laser pulses at optical frequencies enable extracting electrons from solid-state materials via photoemission. Ultimately, the time scales that control the photoemission are given by the carrier-envelope phase which can be nowadays controlled with a precision of few attoseconds [187]. Such photoemission processes can form the basis for femtosecond sources of

electronic currents, which can be utilized for example in ultrafast electron microscopy [188].

Furthermore, it has become possible to generate very strong, few-cycle THz transients with coherent control over their carrier-envelope phase [185]. Under the action of such strong THz electromagnetic field transients, electrons in a crystal are directly accelerated in reciprocal space [185, 189, 190]. Because the frequency of the THz light-field approaches the ballistic and phase scattering rates, the electrons can be driven across a large fraction of the Brillouin zone in a phase coherent manner. By contrast, today's high-frequency devices operate at microwave frequencies, where the electron motion is diffusive on the timescale of the electric field oscillation. Topological surface states with their helical spin-momentum locking and corresponding suppression of backscattering may be particularly suited to carry light-driven currents at THz frequencies [62, 85].

For very strong optical excitation, the light-field cannot be regarded as a small perturbation to the crystal field, and the light-field-driven change of the electron wave number during the optical cycle can dominate the overall light-matter interaction. In this regime, the optical field $\boldsymbol{E}(t)$ changes the electron wavevector $\boldsymbol{k}$ according to [189, 191]

$$\frac{d\boldsymbol{k}}{dt} = -\frac{e}{\hbar}\boldsymbol{E}(t), \tag{6}$$

where $\hbar$ denotes the reduced Planck constant and e is the elementary charge. As a consequence, the light-field drives electron trajectories in reciprocal space, which are controlled by the phase, polarization and magnitude of the optical field. This stands in contrast to photocurrent studies at moderate light fields. Here, the experimental timescales are limited by the duration of the laser pulse (envelope), since the photocarrier generation is driven by vertical optical transitions, governed by the cycle-averaged light intensity. The transition between the strong and weak-field regime occurs when the characteristic energy scale of light-matter interaction, for example given by the ponderomotive energy [192], becomes comparable or larger than the photon energy [80]. In particular, if E is large enough such that the electron traverses the Brillouin zone before scattering takes place, Bragg reflection occurs, and the electron traverses the Brillouin zone again. This leads to dynamical Bloch oscillations in reciprocal space which translate into ultrafast oscillating currents in real space. For intense THz excitation of semiconductors and dielectrics, it has been shown that coupled intraband acceleration and multiphoton interband transitions lead to an extremely nonlinear THz response enabling high-harmonic generation up to several tens of the fundamental frequency [185, 189, 190]. For two-dimensional van der Waal materials, the nonlinear properties may be significantly modified by the reduced symmetries, valley physics, and enhanced many-body interactions. For example, high-harmonic generation from monolayer MoS_2 exhibits strong contributions from the Berry curvature that manifest in even-order peaks in the high-harmonic generation spectrum [193].

Graphene is a promising candidate for light-field-driven electronics from the THz to the optical frequency regime due to its universal broadband response, high electron mobility, fast response time, weak screening and high damage threshold [194–197]. Optical excitation by few-cycle laser pulses can effectively break the inversion symmetry of graphene resulting in a carrier-envelope phase (CEP)-controlled current [80]. In the perturbative regime such a current can arise, for example, from coherent control of the interband excitation pathway in a multiphoton experiment, and the current scales monotonically with a power law (cf. Section 2) [116, 117]. For a strong near-infrared excitation, Higuchi et al. showed that sub-cycle laser pulses induce a current in graphene which is controlled by the carrier-envelope phase of the optical pulse. They demonstrated that the sign of the current reverses at an optical peak field of about 2 Vnm^{-1}. This reversal was interpreted as a transition to the strong-field regime where the electron dynamics are dominated by Landau-Zener-Stückelberg interference of trajectories in reciprocal space [80, 81]. It is worth noting that, because of graphene's peculiar band structure, the response is highly nonlinear [86, 198] and the required field strength to achieve light-field-driven dynamics is about one order of magnitude smaller than that for solid-state dielectrics [82, 199]. Therefore, the strong-field regime could be reached at moderate laser power with a high repetition rate laser oscillator, which is advantageous for optoelectronic applications. In a subsequent study, a pulsed control laser beam, orthogonally polarized to the driving pulses, was introduced [200]. The resulting elliptically polarized driving field allows controlling the electron's trajectory in the full two-dimensional reciprocal space via the phase delay between the two pulses.

Nowadays, few-cycle to sub-cycle THz transients with field strength on the order of several $MVcm^{-1}$ are readily available from table top sources [185]. Compared to optical frequencies, the THz field oscillations are two orders of magnitude slower, which opens an interesting regime for the coherent control of currents in solids. If the intrinsic scattering times become comparable to the oscillation period, electrons will be accelerated to sizeable kinetic energies already at moderate electric field strength. For example, the ponderomotive energy of a free electron driven by a 1 THz wave with a peak field of 0.3 $MVcm^{-1}$ reaches about 1 eV within one half cycle (500 fs) [185].

Furthermore, the combination of a picosecond THz pump and a femtosecond optical probe pulse allows monitoring the electron dynamics at a sub-cycle resolution [185].

In this respect, Reimann et al. demonstrated that the transient electron distribution at the surface of a topological insulator crystal after a pulsed THz excitation can directly be imaged in a tr-ARPES experiment [85] (Figure 6A). First, the topological insulator Bi_2Te_3 is excited by a linearly polarized THz pump pulse ($E_{peak} \sim 3$ kVcm^{-1}). Subsequently, the transient electron dynamics at the crystal surface are directly imaged using tr-ARPES with ultraviolet probe pulses of 100 fs duration. For a p-polarized THz excitation, streaking of the photoemitted electrons by the THz pump field is observed. By contrast, for a s-polarized THz excitation, surface state electrons are coherently accelerated along the surface plane by the THz transient. The resulting tilted Fermi surface is directly evident from the photoemission maps (Figure 6B–G). Intriguingly, the linear Dirac dispersion corresponds to an acceleration process which is quasi inertia-free because of the constant group velocity of Dirac fermions. By comparing the observed shift of the Fermi surface with a Boltzmann transport model, a momentum scattering time larger than 1 ps, an effective surface current density of 2 Acm^{-1}, and a ballistic excursion length on the order of several hundred nanometers were inferred for the topological surface states. Such ballistic transport controlled by optical fields may enable all-coherent currents in electronic devices at terahertz or even petahertz rates.

5 Future directions

For future applications, van der Waals materials can be integrated into on-chip THz circuits based on photoconductive switches. In this way, light-driven currents in nanoscale devices and materials can be directly studied with the highest temporal time resolution (hundreds of femtoseconds) [201–205]. In this context, the ultrafast dynamics of light-driven currents in van der Waals materials have been elucidated in the weak field regime so far, including thermoelectric currents and THz generation in graphene [57, 139, 206, 207], ultrafast carrier dynamics in MoS_2 [42], topological surface currents in Bi_2Se_3 [62, 66],
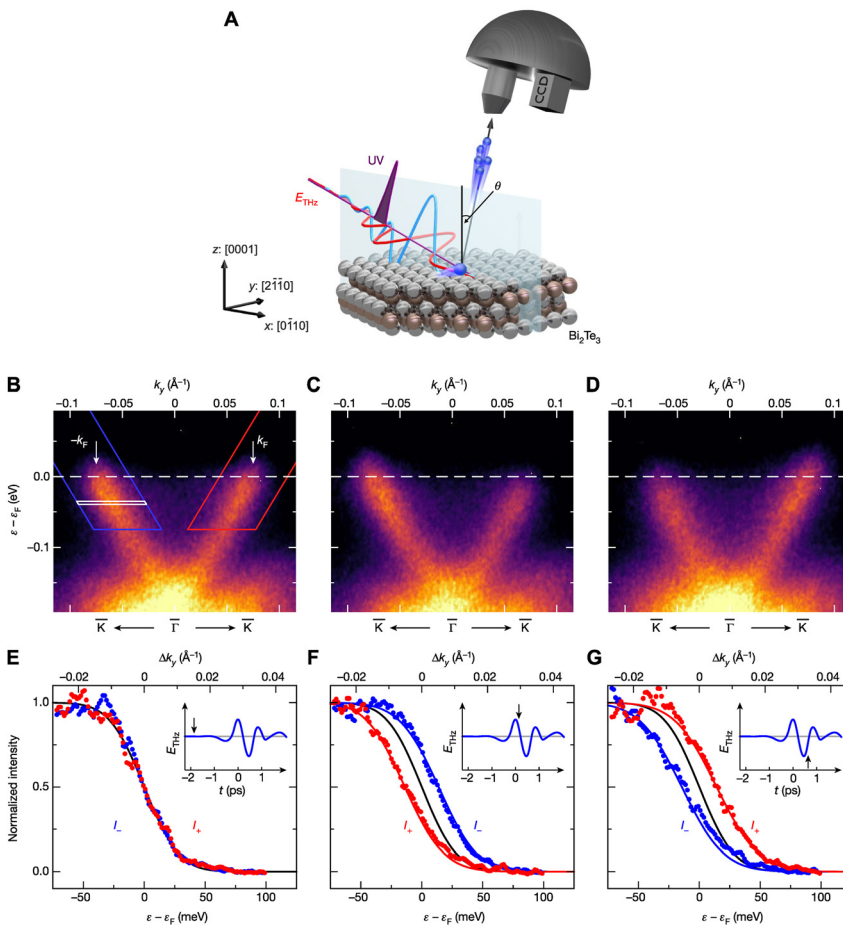

Figure 6: Light-wave-driven THz currents in topological insulator Bi_2Te_3. (A) An intense picosecond THz pulse red waveform, s-polarization; blue waveform, p-polarization) interacts with surface state electrons in Bi_2Te_3. A femtosecond time-delayed UV-pulse (violet) photoemits the surface electrons. In this way, snapshots of the time-resolved band structure are reconstructed as function of the THz pump field. (B) Photoemission map before the arrival of the THz field. The topological surface state shows a linear dispersion. (C) The first positive peak of the THz pulse accelerates the electron distribution towards −k. (D) The negative peak of the THz pulse accelerates the electron distribution towards+k. (E)–(G) Intensity distributions along the left (blue circles) and right (red circles) branches of the Dirac cone, respectively. Insets: reconstructed electric field, with the black arrows indicating the delay times of the corresponding photoemission maps. Reproduced with permission [85]. Copyright 2019, Nature Publishing Group.

and a claimed light-induced anomalous Hall effect in graphene [208]. In a recent study, the above THz spectroscopy was further developed to directly probe the THz conductivity of the Dirac fluid in graphene in an on-chip manner [209]. Overall, such on-chip schemes provide a powerful tool to study light-induced carrier dynamics in nanoscopic van der Waals materials without the constraints imposed by the limited spatial resolution of typical far-field measurements. The integration of van der Waals materials into plasmonic circuits can enable miniaturization of light-wave circuits beyond the diffraction limit [87, 210]. As far as the interaction of strong light-fields with van der Waals materials is concerned, several theoretical studies suggest that few- and sub-cycle optical and THz pulses may enable to directly control the k-space evolution of the charge carriers in atomistic and topological van der Waals materials [211–215], thereby overcoming the general problem in narrow-band-gap bulk materials of light absorption and screening by free charge carriers.

References

[1] J. A. Wilson, A. D. Yoffe, *Adv. Phys.*, vol. 18, p. 193, 1969.
[2] A. Kuc, N. Zibouche, T. Heine, *Phys. Rev. B*, vol. 83, 2011, Art no. 245213.
[3] A. H. Castro Neto, F. Guinea, N. M. R. Peres, K. S. Novoselov, A. K. Geim, *Rev. Mod. Phys.*, vol. 81, p. 109, 2009.
[4] K. S. Novoselov, A. Mishchenko, A. Carvalho, A. H. C. Neto, *Science*, vol. 353 p. aac9439, 2016.
[5] M. Chhowalla, H. S. Shin, G. Eda, L. J. Li, K. P. Loh, H. Zhang, *Nat. Chem.*, vol. 5, p. 263, 2013.
[6] H. Zhang, C. X. Liu, X. L. Qi, X. Dai, Z. Fang, S. C. Zhang, *Nat. Phys.*, vol. 5, p. 438, 2009.
[7] J. C. W. Song, N. M. Gabor, *Nat. Nanotechnol.*, vol. 13, p. 986, 2018.
[8] B. Miller, A. Steinhoff, B. Pano, et al., *Nano Lett.*, vol. 17, p. 5229, 2017.
[9] J. Kiemle, F. Sigger, M. Lorke, et al., *Phys. Rev. B*, vol. 101, 2020, Art no. 121404.
[10] P. Rivera, J. R. Schaibley, A. M. Jones, et al., *Nat. Commun.*, vol. 6, p. 6242, 2015.
[11] A. H. MacDonald, *Physics*, vol. 12, 2019. https://doi.org/10.1103/physics.12.12.
[12] K. Tran, G. Moody, F. Wu, et al., *Nature*, vol. 567, p. 71, 2019.
[13] K. L. Seyler, P. Rivera, H. Yu, et al., *Nature*, vol. 567, p. 66, 2019.
[14] Q. H. Wang, K. Kalantar-Zadeh, A. Kis, J. N. Coleman, M. S. Strano, *Nat. Nanotechnol.*, vol. 7, p. 699, 2012.
[15] K. F. Mak, J. Shan, *Nat. Photon.*, vol. 10, p. 216, 2016.
[16] G. Wang, A. Chernikov, M. M. Glazov, et al., *Rev. Mod. Phys.*, vol. 90, 2018, Art no. 021001.
[17] L. Liu, E. J. Lenferink, G. Wei, T. K. Stanev, N. Speiser, N. P. Stern, *ACS Appl. Mater. Interfaces*, vol. 11, p. 3334, 2019.
[18] H. Yuan, X. Wang, B. Lian, et al., *Nat. Nanotechnol.*, vol. 9, p. 851, 2014.
[19] E. Barré, J. A. C. Incorvia, S. H. Kim, et al., *Nano Lett.*, vol. 19, p. 770, 2019.
[20] K. F. Mak, K. L. McGill, J. Park, P. L. McEuen, *Science*, vol. 344, p. 1489, 2014.
[21] X. X. Zhang, Y. Lai, E. Dohner, et al., *Phys. Rev. Lett.*, vol. 122, 2019, Art no. 127401.
[22] A. Steinhoff, M. Rösner, F. Jahnke, T. O. Wehling, C. Gies, *Nano Lett.*, vol. 14, p. 3743, 2014.
[23] A. Chernikov, C. Ruppert, H. M. Hill, A. F. Rigosi, T. F. Heinz, *Nat. Photon.*, vol. 9, p. 466, 2015.
[24] R. Schmidt, G. Berghäuser, R. Schneider, et al., *Nano Lett.*, vol. 16, p. 2945, 2016.
[25] E. A. A. Pogna, M. Marsili, D. De Fazio, et al., *ACS Nano*, vol. 10, p. 1182, 2016.
[26] S. Ulstrup, A. G. Čabo, J. A. Miwa, et al., *ACS Nano*, vol. 10, p. 6315, 2016.
[27] C. Ruppert, A. Chernikov, H. M. Hill, A. F. Rigosi, T. F. Heinz, *Nano Lett.*, vol. 17, p. 644, 2017.
[28] J. Klein, A. Kerelsky, M. Lorke, et al., *Appl. Phys. Lett.*, vol. 115, 2019, Art no. 261603.
[29] M. Florian, M. Hartmann, A. Steinhoff, et al., *Nano Lett.*, vol. 18, p. 2725, 2018.
[30] C. Ruppert, J. Lohrenz, S. Thunich, M. Betz, *Opt. Lett.*, vol. 37, p. 3879, 2012.
[31] K. F. Mak, D. Xiao, J. Shan, *Nat. Photon.*, vol. 12, p. 451, 2018.
[32] G. Plechinger, P. Nagler, A. Arora, et al., *Nat. Commun.*, vol. 7, 2016, Art no. 12715.
[33] E. J. McCormick, M. J. Newburger, Y. K. Luo, et al., *2D Mater*, vol. 5, 2017, Art no. 011010.
[34] M. Ersfeld, F. Volmer, P. M. M. C. de Melo, et al., *Nano Lett.*, vol. 19, p. 4083, 2019.
[35] X. Song, S. Xie, K. Kang, J. Park, V. Sih, *Nano Lett.*, vol. 16, p. 5010, 2016.
[36] B. T. Zhou, K. Taguchi, Y. Kawaguchi, Y. Tanaka, K. T. Law, *Commun. Phys.*, vol. 2, p. 26, 2019.
[37] K. Hao, G. Moody, F. Wu, et al., *Nat. Phys.*, vol. 12, p. 677, 2016.
[38] L. Yuan, T. F. Chung, A. Kuc, et al., *Sci. Adv.*, vol. 4, 2018, Art no. e1700324.
[39] H. Chen, X. Wen, J. Zhang, et al., *Nat. Commun.*, vol. 7, 2016, Art no. 12512.
[40] M. Palummo, M. Bernardi, J. C. Grossman, *Nano Lett.*, vol. 15, p. 2794, 2015.
[41] C. Robert, D. Lagarde, F. Cadiz, et al., *Phys. Rev. B*, vol. 93, 2016, Art no. 205423.
[42] E. Parzinger, M. Hetzl, U. Wurstbauer, A. W. Holleitner, *Npj 2D Mater. Appl.*, vol. 1, p. 1, 2017.

[43] L. Waldecker, R. Bertoni, H. Hübener, et al., *Phys. Rev. Lett.*, vol. 119, 2017, Art no. 036803.

[44] M. Buscema, M. Barkelid, V. Zwiller, H. S. J. van der Zant, G. A. Steele, A. Castellanos-Gomez, *Nano Lett.*, vol. 13, p. 358, 2013.

[45] M. Fontana, T. Deppe, A. K. Boyd, et al., *Sci. Rep.*, vol. 3, p. 1, 2013.

[46] O. Lopez-Sanchez, D. Lembke, M. Kayci, A. Radenovic, A. Kis, *Nat. Nanotechnol.*, vol. 8, p. 497, 2013.

[47] B. W. H. Baugher, H. O. H. Churchill, Y. Yang, P. Jarillo-Herrero, *Nat. Nanotechnol.*, vol. 9, p. 262, 2014.

[48] M. M. Furchi, D. K. Polyushkin, A. Pospischil, T. Mueller, *Nano Lett.*, vol. 14, p. 6165, 2014.

[49] Y. Zhang, H. Li, L. Wang, et al., *Sci. Rep.*, vol. 5, p. 1, 2015.

[50] H. Wang, C. Zhang, W. Chan, S. Tiwari, F. Rana, *Nat. Commun.*, vol. 6, p. 8831, 2015.

[51] Z. Yin, H. Li, H. Li, et al., *ACS Nano*, vol. 6, p. 74, 2012.

[52] S. Cha, M. Noh, J. Kim, et al., *Nat. Nanotechnol.*, vol. 13, p. 910, 2018.

[53] M. Massicotte, F. Vialla, P. Schmidt, et al., *Nat. Commun.*, vol. 9, p. 1633, 2018.

[54] M. Massicotte, P. Schmidt, F. Vialla, et al., *Nat. Nanotechnol.*, vol. 11, p. 42, 2016.

[55] D. Kufer, I. Nikitskiy, T. Lasanta, G. Navickaite, F. H. L. Koppens, G. Konstantatos, *Adv. Mater.*, vol. 27, p. 176, 2015.

[56] F. H. L. Koppens, T. Mueller, P. Avouris, A. C. Ferrari, M. S. Vitiello, M. Polini, *Nat. Nanotechnol.*, vol. 9, p. 780, 2014.

[57] A. Brenneis, F. Schade, S. Drieschner, et al., *Sci. Rep.*, vol. 6, 2016, Art no. 35654.

[58] A. Junck, G. Refael, F. von Oppen, *Phys. Rev. B*, vol. 88, 2013, Art no. 075144.

[59] P. Hosur, *Phys. Rev. B*, vol. 83, 2011, Art no. 035309.

[60] C. Jozwiak, C.-H. Park, K. Gotlieb, et al., *Nat. Phys.*, vol. 9, p. 293, 2013.

[61] J. W. McIver, D. Hsieh, H. Steinberg, P. Jarillo-Herrero, N. Gedik, *Nat. Nanotechnol.*, vol. 7, p. 96, 2012.

[62] C. Kastl, C. Karnetzky, H. Karl, A. W. Holleitner, *Nat. Commun.*, vol. 6, p. 6617, 2015.

[63] A. Crepaldi, B. Ressel, F. Cilento, et al., *Phys. Rev. B*, vol. 86, 2012, Art no. 205133.

[64] D. Hsieh, F. Mahmood, J. W. McIver, D. R. Gardner, Y. S. Lee, N. Gedik, *Phys. Rev. Lett.*, vol. 107, 2011, Art no. 077401.

[65] K. Kuroda, J. Reimann, K. A. Kokh, et al., *Phys. Rev. B*, vol. 95, 2017, Art no. 081103.

[66] C. Kastl, C. Karnetzky, A. Brenneis, F. Langrieger, A. W. Holleitner, *IEEE J. Sel. Top. Quant. Electron.*, vol. 23, 2017, Art no. 8700305.

[67] L. Braun, G. Mussler, A. Hruban, et al., *Nat. Commun.*, vol. 7, 2016, Art no. 13259.

[68] A. Crepaldi, F. Cilento, B. Ressel, et al., *Phys. Rev. B*, vol. 88, 2013, Art no. 121404.

[69] J. Reimann, J. Güdde, K. Kuroda, E. V. Chulkov, U. Höfer, *Phys. Rev. B*, vol. 90, 2014, Art no. 081106.

[70] K. Kuroda, J. Reimann, J. Güdde, U. Höfer, *Phys. Rev. Lett.*, vol. 116, 2016, Art no. 076801.

[71] J. A. Sobota, S. L. Yang, D. Leuenberger, et al., *Phys. Rev. Lett.*, vol. 113, 2014, Art no. 157401.

[72] C. Kastl, P. Seifert, X. He, K. Wu, Y. Li, A. W. Holleitner, *2D Mater*, vol. 2, 2015, Art no. 024012.

[73] J. Kellner, M. Eschbach, J. Kampmeier, et al., *Appl. Phys. Lett.*, vol. 107, 2015, Art no. 251603.

[74] X. He, T. Guan, X. Wang, et al., *Appl. Phys. Lett.*, vol. 101, 2012, Art no. 123111.

[75] S. Ciocys, T. Morimoto, R. Mori, et al., *Npj Quant. Mater.*, vol. 5, p. 1, 2020.

[76] J. Sánchez-Barriga, M. Battiato, E. Golias, et al., *Appl. Phys. Lett.*, vol. 110, 2017, Art no. 141605.

[77] M. Neupane, S.-Y. Xu, Y. Ishida, et al., *Phys. Rev. Lett.*, vol. 115, 2015, Art no. 116801.

[78] P. Seifert, K. Vaklinova, K. Kern, M. Burghard, A. W. Holleitner, *Nano Lett.*, vol. 17, p. 973, 2017.

[79] P. Seifert, K. Vaklinova, S. Ganichev, K. Kern, M. Burghard, A. W. Holleitner, *Nat. Commun.*, vol. 9, p. 331, 2018.

[80] T. Higuchi, C. Heide, K. Ullmann, H. B. Weber, P. Hommelhoff, *Nature*, vol. 550, p. 224, 2017.

[81] C. Heide, T. Boolakee, T. Higuchi, H. B. Weber, P. Hommelhoff, *New J. Phys.*, vol. 21, 2019, Art no. 045003.

[82] A. Schiffrin, T. Paasch-Colberg, N. Karpowicz, et al., *Nature*, vol. 493, p. 70, 2013.

[83] M. Garg, M. Zhan, T. T. Luu, et al., *Nature*, vol. 538, p. 359, 2016.

[84] A. J. Garzón-Ramírez, I. Franco, *Phys. Rev. B*, vol. 98, 2018, Art no. 121305.

[85] J. Reimann, S. Schlauderer, C. P. Schmid, et al., *Nature*, vol. 562, p. 396, 2018.

[86] M. M. Glazov, S. D. Ganichev, *Phys. Rep.*, vol. 535, p. 101, 2014.

[87] A. Politano, L. Viti, M. S. Vitiello, *APL Mater.*, vol. 5, 2017, Art no. 035504.

[88] V. I. Belinicher, B. I. Sturman, *Sov. Phys. Uspekhi*, vol. 23, p. 199, 1980.

[89] S. D. Ganichev, W. Prettl, *J. Phys. Condens. Matter*, vol. 15, p. R935, 2003.

[90] S. A. Tarasenko, *Phys. Rev. B*, vol. 83, 2011, Art no. 035313.

[91] S. A. Tarasenko, *JETP Lett.*, vol. 85, p. 182, 2007.

[92] R. H. Silsbee, *J. Phys. Condens. Matter*, vol. 16, p. R179, 2004.

[93] K. N. Okada, N. Ogawa, R. Yoshimi, et al., *Phys. Rev. B*, vol. 93, 2016, Art no. 081403.

[94] H. Plank, S. D. Ganichev, *Solid-State Electron.*, vol. 147, p. 44, 2018.

[95] H. Plank, S. N. Danilov, V. V. Bel'kov, et al., *J. Appl. Phys.*, vol. 120, 2016, Art no. 165301.

[96] P. Olbrich, L. E. Golub, T. Herrmann, et al., *Phys. Rev. Lett.*, vol. 113, 2014, Art no. 096601.

[97] J. Duan, N. Tang, X. He, et al., *Sci. Rep.*, vol. 4, p. 4889, 2015.

[98] S. Y. Hamh, S. H. Park, S. K. Jerng, J. H. Jeon, S. H. Chun, J. S. Lee, *Phys. Rev. B*, vol. 94, 2016, Art no. 161405.

[99] Y. Q. Huang, Y. X. Song, S. M. Wang, I. A. Buyanova, W. M. Chen, *Nat. Commun.*, vol. 8, 2017, Art no. 15401.

[100] J. Quereda, T. S. Ghiasi, J. S. You, J. van den Brink, B. J. van Wees, C. H. van der Wal, *Nat. Commun.*, vol. 9, p. 3346, 2018.

[101] Y. J. Zhang, T. Ideue, M. Onga, et al., *Nature*, vol. 570, p. 349, 2019.

[102] Y. B. Lyanda-Geller, S. Li, A. V. Andreev, *Phys. Rev. B*, vol. 92, 2015, Art no. 241406.

[103] N. Ogawa, *Phys. Rev. B*, vol. 90, 2014, https://doi.org/10.1103/PhysRevB.90.125122.

[104] F. de Juan, A. G. Grushin, T. Morimoto, J. E. Moore, *Nat. Commun.*, vol. 8, 2017, Art no. 15995.

[105] E. J. König, H. Y. Xie, D. A. Pesin, A. Levchenko, *Phys. Rev. B*, vol. 96, 2017, Art no. 075123.

[106] L. E. Golub, E. L. Ivchenko, B. Z. Spivak, *JETP Lett.*, vol. 105, p. 782, 2017.

[107] L. E. Golub, E. L. Ivchenko, *Phys. Rev. B*, vol. 98, 2018, Art no. 075305.

[108] C. Jiang, V. A. Shalygin, V. Y. Panevin, et al., *Phys. Rev. B*, vol. 84, 2011, Art no. 125429.

[109] J. Karch, C. Drexler, P. Olbrich, et al., *Phys. Rev. Lett.*, vol. 107, 2011, Art no. 276601.

[110] H. Plank, J. Pernul, S. Gebert, et al., *Phys. Rev. Mater.*, vol. 2, p. 024202, 2018.

[111] S. Y. Xu, Q. Ma, H. Shen, et al., *Nat. Phys.*, vol. 14, p. 900, 2018.

[112] Q. Ma, S. Y. Xu, C. K. Chan, et al., *Nat. Phys.*, vol. 13, p. 842, 2017.

[113] H. Plank, L. E. Golub, S. Bauer, et al., *Phys. Rev. B*, vol. 93, 2016, Art no. 125434.

[114] S. D. Ganichev, D. Weiss, J. Eroms, *Ann. Phys.*, vol. 529, 2017, Art no. 1600406.

[115] P. A. Obraztsov, T. Kaplas, S. V. Garnov, M. Kuwata-Gonokami, A. N. Obraztsov, Y. P. Svirko, *Sci. Rep.*, vol. 4, p. 4007, 2015.

[116] J. Rioux, J. E. Sipe, *Phys. E Low-Dimens. Syst. Nanostruct.*, vol. 45, p. 1, 2012.

[117] D. Sun, C. Divin, J. Rioux, et al., *Nano Lett.*, vol. 10, p. 1293, 2010.

[118] A. Haché, Y. Kostoulas, R. Atanasov, J. L. P. Hughes, J. E. Sipe, H. M. van Driel, *Phys. Rev. Lett.*, vol. 78, p. 306, 1997.

[119] M. Betz, L. Costa, M. Spasenovic, A. D. Bristow, H. M. van Driel, *Phys. Status Solidi C*, vol. 5, p. 340, 2008.

[120] C. Ruppert, S. Thunich, G. Abstreiter, A. Fontcuberta i Morral, A. W. Holleitner, M. Betz, *Nano Lett.*, vol. 10, p. 1799, 2010.

[121] R. Atanasov, A. Haché, J. L. P. Hughes, H. M. van Driel, J. E. Sipe, *Phys. Rev. Lett.*, vol. 76, p. 1703, 1996.

[122] P. T. Mahon, R. A. Muniz, J. E. Sipe, *Phys. Rev. B*, vol. 100, p. 075203, 2019.

[123] S. Thunich, C. Ruppert, A. W. Holleitner, M. Betz, *Appl. Phys. Lett.*, vol. 101, 2012, Art no. 251119.

[124] E. J. Mele, P. Král, D. Tománek, *Phys. Rev. B*, vol. 61, p. 7669, 2000.

[125] Q. Cui, H. Zhao, *ACS Nano*, vol. 9, p. 3935, 2015.

[126] R. W. Newson, J. M. Ménard, C. Sames, M. Betz, H. M. van Driel, *Nano Lett.*, vol. 8, p. 1586, 2008.

[127] R. A. Muniz, J. E. Sipe, *Phys. Rev. B*, vol. 89, 2014, Art no. 205113.

[128] R. A. Muniz, J. E. Sipe, *Phys. Rev. B*, vol. 91, 2015, Art no. 085404.

[129] D. Côté, J. M. Fraser, M. DeCamp, P. H. Bucksbaum, H. M. van Driel, *Appl. Phys. Lett.*, vol. 75, p. 3959, 1999.

[130] R. Bertoni, C. W. Nicholson, L. Waldecker, et al., *Phys. Rev. Lett.*, vol. 117, 2016, Art no. 277201.

[131] J. Güdde, M. Rohleder, T. Meier, S. W. Koch, U. Höfer, *Phys. Status Solidi C*, vol. 6, p. 461, 2009.

[132] C. L. Smallwood, R. A. Kaindl, A. Lanzara, *EPL Europhys. Lett.*, vol. 115, 2016, Art no. 27001.

[133] J. Güdde, M. Rohleder, T. Meier, S. W. Koch, U. Höfer, *Science*, vol. 318, p. 1287, 2007.

[134] T. Oka, H. Aoki, *Phys. Rev. B*, vol. 79, 2009, Art no. 081406.

[135] Z. Ji, G. Liu, Z. Addison, et al., *Nat. Mater.*, vol. 18, p. 955, 2019.

[136] P. Seifert, M. Kundinger, G. Shi, et al., *Phys. Rev. Lett.*, vol. 122, 2019, Art no. 146804.

[137] J. Kiemle, P. Seifert, A. W. Holleitner, C. Kastl, *Phys. Status Solidi B*, 2020, n/a, Art no. 2000033. https://doi.org/10.1002/pssb.202000033.

[138] C. Kastl, T. Guan, X. Y. He, K. H. Wu, Y. Q. Li, A. W. Holleitner, *Appl. Phys. Lett.*, vol. 101, 2012, Art no. 251110.

[139] L. Prechtel, L. Song, D. Schuh, P. Ajayan, W. Wegscheider, A. W. Holleitner, *Nat. Commun.*, vol. 3, p. 646, 2012.

[140] M. Stallhofer, C. Kastl, M. Brändlein, et al., *Phys. Rev. B*, vol. 86, 2012, Art no. 115313.

[141] A. Avsar, D. Unuchek, J. Liu, et al., *ACS Nano*, vol. 11, 2017, Art no. 11678.

[142] D. Xiao, M. C. Chang, Q. Niu, *Rev. Mod. Phys.*, vol. 82, p. 1959, 2010.

[143] N. A. Sinitsyn, *J. Phys. Condens. Matter*, vol. 20, 2007, Art no. 023201.

[144] M. Gradhand, D. V. Fedorov, F. Pientka, P. Zahn, I. Mertig, B. L. Györffy, *J. Phys. Condens. Matter*, vol. 24, 2012, Art no. 213202.

[145] D. Xiao, G. B. Liu, W. Feng, X. Xu, W. Yao, *Phys. Rev. Lett.*, vol. 108, 2012, Art no. 196802.

[146] T. Y. T. Hung, K. Y. Camsari, S. Zhang, P. Upadhyaya, Z. Chen, *Sci. Adv.*, vol. 5, 2019, Art no. eaau6478.

[147] T. Yu, M. W. Wu, *Phys. Rev. B*, vol. 93, 2016, Art no. 045414.

[148] M. I. Dyakonov, A. V. Khaetskii, in *Spin Phys. Semicond.*, M. I. Dyakonov, Ed., Springer, Berlin, Heidelberg, pp. 211–243, 2008.

[149] W. Y. Shan, *Phys. Rev. B*, vol. 88, 2013, Art no. 125301.

[150] Z. Wu, B. T. Zhou, X. Cai, et al., *Nat. Commun.*, vol. 10, p. 611, 2019.

[151] M. M. Glazov, L. E. Golub, ArXiv200405091, *Cond-Mat*, 2020.

[152] N. Nagaosa, J. Sinova, S. Onoda, A. H. MacDonald, N. P. Ong, *Rev. Mod. Phys.*, vol. 82, p. 1539, 2010.

[153] E. Lorchat, S. Azzini, T. Chervy, et al., *ACS Photon.*, vol. 5, p. 5047, 2018.

[154] A. Steinhoff, M. Florian, M. Rösner, G. Schönhoff, T. O. Wehling, F. Jahnke, *Nat. Commun.*, vol. 8, p. 1166, 2017.

[155] K. Yao, A. Yan, S. Kahn, et al., *Phys. Rev. Lett.*, vol. 119, 2017, Art no. 087401.

[156] M. Onga, Y. Zhang, T. Ideue, Y. Iwasa, *Nat. Mater.*, vol. 16, p. 1193, 2017.

[157] N. Lundt, Ł. Dusanowski, E. Sedov, et al., *Nat. Nanotechnol.*, vol. 14, p. 770, 2019.

[158] A. Kormányos, V. Zólyomi, V. I. Fal'ko, G. Burkard, *Phys. Rev. B*, vol. 98, 2018, Art no. 035408.

[159] J. Lee, K. F. Mak, J. Shan, *Nat. Nanotechnol.*, vol. 11, p. 421, 2016.

[160] Y. Li, Y. Rao, K. F. Mak, et al., *Nano Lett.*, vol. 13, p. 3329, 2013.

[161] K. H. Kim, H. W. Lee, *Phys. Rev. B*, vol. 97, 2018, Art no. 235423.

[162] C. Jin, J. Kim, M. I. B. Utama, et al., *Science*, vol. 360, p. 893, 2018.

[163] M. Z. Hasan, C. L. Kane, *Rev. Mod. Phys.*, vol. 82, p. 3045, 2010.

[164] D. Hsieh, Y. Xia, D. Qian, et al., *Nature*, vol. 460, p. 1101, 2009.

[165] Y. Pan, Q. Z. Wang, A. L. Yeats, et al., *Nat. Commun.*, vol. 8, p. 1037, 2017.

[166] D. X. Qu, X. Che, X. Kou, et al., *Phys. Rev. B*, vol. 97, 2018, Art no. 045308.

[167] K. W. Kim, T. Morimoto, N. Nagaosa, *Phys. Rev. B*, vol. 95, 2017, Art no. 035134.

[168] R. Valdés Aguilar, J. Qi, M. Brahlek, et al., *Appl. Phys. Lett.*, vol. 106, 2015, Art no. 011901.

[169] W. Tang, A. Politano, C. Guo, et al., *Adv. Funct. Mater.*, vol. 28, 2018, Art no. 1801786.

[170] Z. K. Liu, L. X. Yang, Y. Sun, et al., *Nat. Mater.*, vol. 15, p. 27, 2016.

[171] B. Yan, C. Felser, *Annu. Rev. Condens. Matter Phys.*, vol. 8, p. 337, 2017.

[172] C. K. Chan, P. A. Lee, K. S. Burch, J. H. Han, Y. Ran, *Phys. Rev. Lett.*, vol. 116, 2016, Art no. 026805.

[173] L. Wu, S. Patankar, T. Morimoto, et al., *Nat. Phys.*, vol. 13, p. 350, 2017.

[174] N. V. Leppenen, E. L. Ivchenko, L. E. Golub, *J. Exp. Theor. Phys.*, vol. 129, p. 139, 2019.

[175] A. A. Soluyanov, D. Gresch, Z. Wang, et al., *Nature*, vol. 527, p. 495, 2015.

[176] Y. Zhang, Y. Sun, B. Yan, *Phys. Rev. B*, vol. 97, 2018, Art no. 041101.

[177] K. Kang, T. Li, E. Sohn, J. Shan, K. F. Mak, *Nat. Mater.*, vol. 18, p. 324, 2019.

[178] Q. Ma, S. Y. Xu, H. Shen, et al., *Nature*, vol. 565, p. 337, 2019.

[179] Z. Z. Du, C. M. Wang, S. Li, H. Z. Lu, X. C. Xie, *Nat. Commun.*, vol. 10, p. 3047, 2019.

[180] S. Onoda, N. Sugimoto, N. Nagaosa, *Phys. Rev. Lett.*, vol. 97, 2006, Art no. 126602.

[181] P. Seifert, F. Sigger, J. Kiemle, et al., *Phys. Rev. B*, vol. 99, 2019, Art no. 161403.

[182] Q. Song, H. Wang, X. Xu, et al., *RSC Adv.*, vol, 6, 2016, Art no. 103830.

[183] Q. Wang, J. Li, J. Besbas, et al., *Adv. Sci.*, vol. 5, 2018, Art no. 1700912.

[184] Y. M. Dai, J. Bowlan, H. Li, et al., *Phys. Rev. B*, vol. 92, 2013, Art no. 161104.

[185] T. Kampfrath, K. Tanaka, K. A. Nelson, *Nat. Photon.*, vol. 7, p. 680, 2013.

[186] G. Sansone, L. Poletto, M. Nisoli, *Nat. Photon.*, vol. 5, p. 655, 2011.

[187] M. Krüger, M. Schenk, P. Hommelhoff, *Nature*, vol. 475, p. 78, 2011.

[188] M. Aidelsburger, F. O. Kirchner, F. Krausz, P. Baum, *Proc. Natl. Acad. Sci.*, vol. 107, 2010, Art no. 19714.

[189] D. Golde, M. Kira, T. Meier, S. W. Koch, *Phys. Status Solidi B*, vol. 248, p. 863, 2011.

[190] O. Schubert, M. Hohenleutner, F. Langer, et al., *Nat. Photon.*, vol. 8, p. 119, 2014.

[191] A. Nenciu, G. Nenciu, *Phys. Lett .A*, vol. 78, p. 101, 1980.

[192] H. R. Reiss, *Phys. Rev. A*, vol. 22, p. 1786, 1980.

[193] H. Liu, Y. Li, Y. S. You, S. Ghimire, T. F. Heinz, D. A. Reis, *Nat. Phys.*, vol. 13, p. 262, 2017.

[194] A. Roberts, D. Cormode, C. Reynolds, T. Newhouse-Illige, B. J. LeRoy, A. S. Sandhu, *Appl. Phys. Lett.*, vol. 99, 2011, Art no. 051912.

[195] S. Engels, B. Terrés, A. Epping, et al., *Phys. Rev. Lett.*, vol. 113, 2014, Art no. 126801.

[196] A. B. Kuzmenko, E. van Heumen, F. Carbone, D. van der Marel, *Phys. Rev. Lett.*, vol. 100, 2008, Art no. 117401.

[197] K. J. Tielrooij, L. Piatkowski, M. Massicotte, et al., *Nat. Nanotechnol.*, vol. 10, p. 437, 2015.

[198] S. Mikhailov, in *Carbon Nanotub. Graphene Photonic Appl.*, S. Yamashita, Y. Saito, J.H. Choi, Eds., Woodhead Publishing, pp. 171–221e, 2013.

[199] S. Ghimire, A. D. DiChiara, E. Sistrunk, P. Agostini, L. F. DiMauro, D. A. Reis, *Nat. Phys.*, vol. 7, p. 138, 2011.

[200] C. Heide, T. Higuchi, H. B. Weber, P. Hommelhoff, *Phys. Rev. Lett.*, vol. 121, 2018, Art no. 207401.

[201] M. B. Ketchen, D. Grischkowsky, et al., *Appl. Phys. Lett.*, vol. 48, p. 751, 2018.

[202] D. H. Auston, *Appl. Phys. Lett.*, vol. 26, p. 101, 1975.

[203] F. E. Doany, D. Grischkowsky, C. C. Chi, *Appl. Phys. Lett.*, vol. 50, p. 460, 1987.

[204] C. Karnetzky, P. Zimmermann, C. Trummer, et al., *Nat. Commun.*, vol. 9, p. 2471, 2018.

[205] N. Fernandez, P. Zimmermann, P. Zechmann, M. Wörle, R. Kienberger, A. W. Holleitner, in *Ultrafast Phenom. Nanophotonics XXIII*, International Society For Optics And Photonics, 2019, Art no. 109160R.

[206] N. Hunter, A. S. Mayorov, C. D. Wood, et al., *Nano Lett.*, vol. 15, p. 1591, 2015.

[207] A. Brenneis, L. Gaudreau, M. Seifert, et al., *Nat. Nanotechnol.*, vol. 10, p. 135, 2015.

[208] J. W. McIver, B. Schulte, F. U. Stein, et al., *Nat. Phys.*, vol. 16, p. 38, 2020.

[209] P. Gallagher, C. S. Yang, T. Lyu, et al., *Science*, vol. 364, p. 158, 2019.

[210] K. Y. Bliokh, F. J. Rodríguez-Fortuño, A. Y. Bekshaev, Y. S. Kivshar, F. Nori, *Opt. Lett.*, vol. 43, p. 963, 2018.

[211] H. K. Kelardeh, V. Apalkov, M. I. Stockman, *Phys. Rev. B*, vol. 93, 2016, Art no. 155434.

[212] S. A. Oliaei Motlagh, J. S. Wu, V. Apalkov, M. I. Stockman, *Phys. Rev. B*, vol. 98, 2018, Art no. 081406.

[213] S. A. Oliaei Motlagh, J. S. Wu, V. Apalkov, M. I. Stockman, *Phys. Rev. B*, vol. 98, 2018, Art no. 125410.

[214] R. E. F. Silva, Á. Jiménez-Galán, B. Amorim, O. Smirnova, M. Ivanov, *Nat. Photon.*, vol. 13, p. 849, 2019.

[215] L. Peralta Gavensky, G. Usaj, C. A. Balseiro, *Phys. Rev. B*, vol. 98, 2018, Art no. 165414.